Two FtsZ proteins orchestrate archaeal cell division through distinct functions in ring assembly and constriction

*Yan Liao[a.], *Solenne Ithurbide[a.], Christian Evenhuis[a.], Jan Löwe[b.] and Iain G. Duggin[a.]

*These authors contributed equally.

a. The ithree institute, University of Technology Sydney, Ultimo, NSW, 2007, Australia.

b. MRC Laboratory of Molecular Biology, Francis Crick Avenue, Cambridge, CB2 0QH, UK.

Address correspondence to Iain G. Duggin (Iain.Duggin@uts.edu.au), Tel: +61 2 9514 8403.

Keywords: FtsZ, tubulin, archaea, cell division, cytokinesis, cell envelope, cell wall, S-layer, cell morphology.

The tubulin homolog FtsZ assembles a cytokinetic ring in bacteria and plays a key role in the machinery that constricts to divide the cells. Many archaea encode two FtsZ proteins from distinct families, FtsZ1 and FtsZ2, of previously unclear functions. Here we show that *Haloferax volcanii* cannot divide properly without either or both, but DNA replication continues, and cells proliferate in alternative ways via remarkable envelope plasticity. FtsZ1 and FtsZ2 co-localize to form the dynamic division ring. However, FtsZ1 can assemble rings independently of FtsZ2, and stabilizes FtsZ2 in the ring, whereas FtsZ2 functions primarily in the constriction mechanism. FtsZ1 also influenced cell shape suggesting it forms a hub-like platform at midcell for the assembly of shape-related systems too. Both FtsZ1 and FtsZ2 are widespread in archaea with a single S-layer envelope, but archaea with a pseudomurein wall and division septum only have FtsZ1. FtsZ1 is therefore likely to provide a fundamental recruitment role in diverse archaea, and FtsZ2 is required for constriction of a flexible S-layer envelope, where an internal constriction force might dominate the division mechanism, in contrast to the single-FtsZ bacteria and archaea that divide primarily by wall ingrowth.

FtsZ is the most conserved bacterial cell division protein and among the first molecules to assemble at the incipient division site. It forms a dynamic ring-like structure around the cell that acts as a platform to initiate recruitment of about a dozen core components and up to ~30 other factors involved in division[1,2]. Within the ring, FtsZ polymerizes dynamically in a GTP-dependent manner near the inner surface of the cytoplasmic membrane, directing the inward synthesis of septal cell wall peptidoglycan to drive cell constriction, and may also provide a direct influence on membrane constriction[3-7]. The septal wall splits to separate the two new cells in a process that is either continuous with septal wall synthesis and ring closure or is activated after the septal cross-wall is complete[8,9].

An *ftsZ* homolog was first identified in several archaea by DNA hybridization[10,11] and GTP-binding screens[12]. Archaeal FtsZ showed GTPase activity *in vitro*[11] and was localized to mid-cell by immunofluorescence[11,13]. In bacteria such as *E. coli*, the actin homolog FtsA forms filaments that, together with ZipA and several regulatory or stabilization proteins, link FtsZ filaments to the inner membrane[2,14]. However, homologs of these and most other bacterial (and eukaryotic) cell division proteins appear to be largely absent in archaea. One exception and likely candidate is the archaeal homolog of SepF, which can polymerize and participates with

47 FtsA in anchoring FtsZ for Gram-positive bacterial division[15], and shows strong phylogenetic
48 association with FtsZ in archaea[16].

49 The first complete archaeal genome sequence, of *Methanocaldococcus jannaschii*,[17] revealed
50 multiple *ftsZ* homologs, whereas almost all bacterial genomes contain only one *ftsZ*. Some
51 archaea do not contain FtsZ, including the phylum Crenarchaeota, where division is instead
52 orchestrated by proteins related to the ESCRT-III complexes involved in membrane
53 remodelling in eukaryotes[18,19]. Many of the archaea that contain FtsZ also have one or more
54 tubulin-superfamily proteins from the CetZ family[20,21]. The genome of the archaeal model
55 organism *Haloferax volcanii*[22] encodes eight tubulin-superfamily proteins—six CetZs, and two
56 FtsZs. Work in *H. volcanii* showed that the CetZs were not individually required for division,
57 but at least one is required for rod cell shape development[20]. In the same study, an FtsZ1-GFP
58 fusion protein was observed to localize at midcell. The results also suggested *H. volcanii* as an
59 excellent model for archaeal cell biology, as it has relatively large and flat cells that show a
60 variety of regulated morphologies and are well-suited to light and electron microscopy[20,23,24].
61 Here we use *H. volcanii* to demonstrate that FtsZ1 and FtsZ2 have different functions in the
62 mechanism of archaeal cell division.

63 Results

64 *Characteristics of two FtsZ families in archaea*

65 We performed a molecular phylogenetic analysis of 149 tubulin-superfamily proteins
66 identified in 60 diverse archaeal genomes. Archaeal FtsZ1, FtsZ2, and the well-studied
67 bacterial/plant FtsZ form three distinct families that are approximately equally divergent from
68 one another (Fig. S1a). A majority of the archaea encoded both an FtsZ1 and an FtsZ2 homolog,
69 including most Euryarchaeota (*e.g.*, Halobacteria, Thermococci and Archaeoglobi) and the
70 DPANN and Asgard superphyla (Table S3). The Crenarchaeota and Thaumarchaeota lacked
71 specific members of the FtsZ families, whereas methanogenic archaea, that characteristically
72 have a pseudomurein wall not found in other species, were found to only possess FtsZ1 (Fig.
73 S1, Table S3).

74 We noticed conserved differences between archaeal FtsZ1 and FtsZ2 that are primarily in the
75 vicinity of the GTPase active site and longitudinal subunit interface in polymers (see
76 Supplementary Results and Discussion, Fig. S1c-e). Conserved motifs were also identified in

77 the N- and C-terminal tails that differed from bacterial/plant FtsZ. These differences are likely
78 to manifest as fundamental functional characteristics of the three FtsZ families but await further
79 detailed investigations.

80 ***Depletion of FtsZ1 or FtsZ2 causes division defects in H. volcanii***

81 Given that *ftsZ* genes are nearly ubiquitous and important for survival in bacteria[25], we first
82 engineered *H. volcanii* strains in which expression of the genomic copy of the *ftsZ1*
83 (HVO_0717) or *ftsZ2* (HVO_0581) gene was placed under the control of the highly specific
84 tryptophan-regulated promoter *p.tna*[26] (Fig. S2); expression of each *ftsZ* could be maintained
85 during strain construction and growth by the inclusion of tryptophan (Trp) in the growth
86 medium, or depleted by placing the cells into medium without Trp. The two corresponding
87 strains grew well in the presence of 2 mM Trp and appeared of approximately normal size and
88 shape (Fig. 1a, 0 h, leftmost panels). However, resuspension of growing cells in liquid medium
89 without Trp caused a large increase in cell size over the 24 h sampling period (biomass doubling
90 times of ~4.4 h over the first 9 h of log growth), as shown by phase-contrast microscopy (Fig.
91 1a) and Coulter cytometry cell-volume distributions (Fig. S3). This is morphologically
92 analogous to the classical bacterial filamentous phenotype[27], and signifies a defect in the
93 regulation or mechanism of cell division in both the *ftsZ1*- and *ftsZ2*-depletion strains. The
94 *ftsZ2* depletion resulted in a stronger division defect (significantly larger cells) compared to the
95 *ftsZ1* depletion (Fig. 1a, S3). Western blotting showed that the cellular amount of FtsZ1 had
96 decreased substantially by ~6-9 h after withdrawal of Trp from the *p.tna-ftsZ1* strain, whereas
97 in the *p.tna-ftsZ2* strain, FtsZ2 had almost completely disappeared after 3 h (Fig. 1b). Whether
98 the cell size difference is due to the different rates of depletion or differing roles and importance
99 of the two FtsZ proteins to cell division is addressed further below.

100 Time-lapse microscopy of growing cells showed some FtsZ1-depleted cells dividing,
101 apparently inefficiently, whereas FtsZ2 depletion appeared to strongly block division (*e.g.*, Fig.
102 1c). After the onset of depletion, some *p.tna-ftsZ2* cells initially developed a constriction but
103 were unable to complete division; the partial constriction then reversed with further cell growth
104 yet had a lingering influence on cell shape (Fig. S4). Later in depletion, budding-like processes
105 were observed that resulted in apparent vesicles or minicells of variable sizes (Video S1, *p.tna-*
106 *ftsZ2*). In some of the enlarged FtsZ1-depleted cells, a small cell fragment appeared at one side
107 of the division plane during cell separation (Fig. 1c, arrow) or in others appeared to be 'carved
108 out' from a cell edge (Video S2). In contrast, FtsZ2-depleted cells were not seen actively

109 dividing, although some showed blebbing from cellular lobes in these very large misshapen
110 cells (Video S3).

111 FtsZ-depleted cells that were re-supplied with Trp at the commencement of time-lapse imaging
112 (FtsZ restoration) showed that the giant cells then became capable of dividing (Fig. 1d, Video
113 S1). Some underwent multiple simultaneous divisions, generating large cells that then
114 underwent further division events to eventually re-establish a population of normal-sized cells.
115 It was also clear that the division process itself was sometimes asymmetric (unilateral), where
116 cell constriction occurs from only one edge (or predominately from one edge), and the plane
117 of division was sometimes noticeably acentral or not straight nor perpendicular to the cell
118 envelope (Video S1). Irregular positioning of division sites may be expected based on the
119 sensitivity of division site positioning mechanisms to cell size and shape[28], and this resulted in
120 noticeable pleomorphology in the progeny.

121 ***DNA composition of H. volcanii cells depleted of FtsZ1 or FtsZ2***

122 To assess the positioning and replication of DNA in cells after depletion of each FtsZ, we
123 stained cells with SYTOX Green (SG) DNA stain. The giant cells showed DNA-SG staining
124 that appeared diffusely present throughout the cytoplasm, similar to the staining intensity and
125 distribution in wild-type cells (Fig. S5a). Flow cytometry showed that DNA-SG fluorescence
126 correlated with the side-scatter signal as a proxy for cell size (Fig. S5b). Some of the largest
127 mutant cells (*e.g.,* after *ftsZ2*-depletion) showed ~100-fold higher DNA-SG fluorescence and
128 side-scatter than wild-type, corresponding to an expected genome copy number of ~2000 or
129 more in the largest mutant cells, compared to the typical polyploidy of ~20 in unmodified *H.*
130 *volcanii*[29]. These results indicate that DNA synthesis continues in approximate proportion to
131 cell biomass increase during inhibition of cell division caused by FtsZ depletion, and are
132 consistent with the previously observed simple correlation between DNA content and cell size
133 in wild-type *H. volcanii*[30] that reflects an absence of distinct cell-cycle phases (Fig. S5b).

134 ***H. volcanii propagates without FtsZ1 and/or FtsZ2***

135 The *p.tna-ftsZ1* and *p.tna-ftsZ2* strains were grown continuously at a range of Trp
136 concentrations (from 0 to 2 mM Trp) and showed an inverse relationship between Trp
137 concentration and cell size (Fig. S6a-b). Since both *ftsZ*-depletion strains could be maintained
138 indefinitely in standard growth medium (Hv-Cab) in the absence of added Trp, we sought to
139 determine whether the *ftsZ* genes were completely dispensable by employing a direct selection

140 procedure to delete each gene. The Δ*ftsZ1* and Δ*ftsZ2* strains were viable and we also made a
141 double deletion (Δ*ftsZ1* Δ*ftsZ2*) and then confirmed the deletions by PCR and genome
142 sequencing. Mid-log cultures had biomass doubling times of 3.08±0.06 h (H26 wild type),
143 3.58±0.27 h (Δ*ftsZ1*), 3.56±0.23 h (Δ*ftsZ2*) and 4.20±0.18 h (Δ*ftsZ1* Δ*ftsZ2*) (mean±95% CI,
144 Fig. S7a). Dilution and agar plating of mid-log samples (OD_{600} = 0.2) showed that the three
145 Δ*ftsZ* strains had 20-25-fold fewer colony forming units (cfu) compared to the wild-type (Fig.
146 2a), consistent with a larger cell size and/or a reduced fraction of viable cells. The Δ*ftsZ* strains
147 displayed very heterogeneously sized and misshapen cells, and a significant quantity of cellular
148 debris (Fig. 2b-c), very similar to the respective *p.tna-ftsZ* strains grown continuously without
149 Trp (Fig. S6a). The Δ*ftsZ2* and Δ*ftsZ1* Δ*ftsZ2* strains showed more severe cell-division defects
150 compared to Δ*ftsZ1*, indicating that FtsZ2 has a limited capacity to support division in the
151 absence of FtsZ1 (Fig. 2b-c). The equally low cfu count of Δ*ftsZ1* therefore suggests FtsZ1
152 may have additional functions that contribute to cell viability. Furthermore, the relatively
153 moderate FtsZ1-depletion cell-division phenotype (Fig. 1a) appears to be largely caused by
154 differing roles of FtsZ1 and FtsZ2 rather than the differences in depletion rate (Fig. 1b).

155 The genome sequence data for H98 and the three knock-out strains showed several small
156 sequence variations of no known or expected consequences (Table S5). We therefore sought
157 to verify the attribution of the above phenotypes specifically to *ftsZ1* and/or *ftsZ2* by
158 reintroducing these genes under control of the *p.tna* promoter on a plasmid (based on pTA962)
159 into the corresponding deletion mutants. In all three cases this successfully complemented the
160 division defects in the presence of 0.2 mM Trp induction or greater (Fig. 2g, S8, S9). At
161 relatively high concentrations of Trp (1 or 2 mM), the strains expressing *ftsZ1* showed some
162 rods or spindle-like cell shapes (investigated further below).

163 The apparent correlation between the appearance of greatly enlarged cells and debris (< 1 μm^3,
164 Fig. 2c) suggested that the largest cells produce cell fragments or disintegrate to form the
165 debris. Interestingly, *ΔftsZ1 ΔftsZ2* also showed a greater frequency of highly elongated
166 filamentous cells (31%), compared to the plate-like cell shapes seen in mid-log cultures of the
167 wild-type and two single *ΔftsZ* strains (< 1% filaments) (Fig. 2b, S7c). *H. volcanii* shapes can
168 be readily influenced by several conditions or stresses[24] (see Supplementary Results and
169 Discussion) and the two major categories of giant cells appear to be the result of division
170 defects in the common plate and rods morphotypes, respectively. The filamentous Δ*ftsZ1*
171 Δ*ftsZ2* cells showed a similar flattened shape profile cells as the wild-type rod- and plate-

172 shaped cells, which are normally ~0.5 μm thick (Fig. 2d, Video S4). However, the giant plate-
173 like cells had lost much of the flatness of the wild-type and displayed multi-lobed ramified 3D
174 morphologies (Fig. 2d, S7b, Video S4), underscoring the remarkable plasticity of the *H.*
175 *volcanii* envelope in the giant cells. This could lead to abiotic division or cell
176 disintegration/fragmentation in a turbulent environment, and account for some of the highly
177 irregular morphologies observed when cells are transferred from liquid to an agarose gel
178 surface (*e.g.*, Fig. 1a, 2b).

179 To further assess the capacity of cells to survive without *ftsZ*, including potential propagation
180 via alternative biotic processes, mid-log samples were transferred to soft-agarose media pads
181 to image cells during growth (Fig. 2e, S7d, Videos S5-S8). Under these conditions, the mutants
182 grew substantially larger (over ~12 h), indicating that cells were structurally stabilized by the
183 gel compared to the prior liquid culture (Fig. 2c). Nevertheless, while some Δ*ftsZ1* cells grew
184 very large (Video S5), others divided, often very acentrally or with a crooked division plane
185 (Video S6). Division was not seen in Δ*ftsZ2* cells, which expanded to extremely large sizes,
186 and rare blebbing was seen (Video S7). Interestingly, the filaments common in Δ*ftsZ1* Δ*ftsZ2*
187 showed substantial polar narrowing and extension (tubulation), followed by fission to produce
188 much smaller fragments (Fig. 2e-f, Video S8). These samples also contained many small
189 particles, which may be the product of the polar tubulation-and-fission or fragmentation in
190 prior culture. The fragmentation, budding, tubulation-and-fission, and, in the case of Δ*ftsZ1,*
191 occasional inaccurate division, appear to result in particles, at least some of which contain
192 DNA (see Fig. S5a), that produce enough viable cells for culture propagation in the absence of
193 normal cell division.

194 ***Overexpression of ftsZ1 or ftsZ2 cause contrasting phenotypes, and cannot properly***
195 ***compensate for loss of the other***

196 If FtsZ1 and FtsZ2 have different roles in division, then overexpression of each could
197 exacerbate aspects of each protein's specific activities and potentially lead to different effects.
198 Furthermore, if overexpression of *ftsZ2* in the *ΔftsZ1* strain, and vice versa, corrects the division
199 defects (*i.e.*, cross-complementation), then this would indicate similar or overlapping functions
200 of the two proteins. FtsZ1 overproduction in the wild-type background caused enlarged cells,
201 indicating inefficient or mis-regulated division (Fig 3). It also caused a change in cell shape,
202 where cells frequently displayed a rod-like appearance or a noticeable taper at one or both poles
203 (Fig. 3c). In contrast, FtsZ2 overproduction resulted in smaller cells than the wild type,

204 indicating that FtsZ2 overproduction stimulates division, with no specific influence on cell
205 shape (Fig. 3).

206 FtsZ1 overproduction provided no detectable recovery to the Δ*ftsZ2* division defect (Fig. 2h,
207 S10), but caused increased debris and some striking spindle-like cell shapes with rather pointy
208 poles or various angular morphologies, as well as very long filamentous cells of approximately
209 normal rod-cell width. The spindly cells therefore appear to be associated with FtsZ1
210 overproduction in the wild-type, Δ*ftsZ1* and Δ*ftsZ2* backgrounds (Fig. 3a, 2g-h, S11). FtsZ2
211 overproduction caused weak complementation of the *ΔftsZ1* division defect (Fig. 2g-h, S8,
212 S10), indicating partial compensation for the missing FtsZ1 or a capacity to take on some of
213 the role(s) of FtsZ1 in division. These findings show that FtsZ1 and FtsZ2 have differing
214 functions, and that FtsZ2 has an essential active role in the constriction mechanism, whereas
215 FtsZ1 has a supporting role. Consistent with this, as *ftsZ1* mutant cultures slowed growth and
216 entered stationary phase, cell size recovered to nearly normal, but this did not occur in *ftsZ2*
217 mutants (Fig. S12). The stationary phase results and effects of *ftsZ* mutants on cell shape are
218 further discussed in the Supplementary Results and Discussion.

219 ***Predicted GTPase active site (T7 loop) residues are essential for FtsZ1 and FtsZ2 functions***

220 FtsZ1 and FtsZ2 both contain the conserved GTP binding domain and catalytic residues in the
221 T7 loop (see Fig. S1d) that are needed for GTP hydrolysis and correct function of FtsZ/tubulin
222 polymers[31,32]. Bacterial FtsZ studies have showed that point mutations of the T7 catalytic
223 residues block GTPase-dependent filament disassembly, thus forming hyper-stable filaments
224 that can co-assemble with the wild-type protein and severely disrupt function[33-35].
225 Overproduction of an equivalent aspartate-to-alanine point mutant of FtsZ1 (D250A,
226 substitution in the T7 loop) inhibited division in *H. volcanii*[20]. To determine whether both
227 FtsZ1 and FtsZ2 require their predicted GTPase catalytic residues for their functions in
228 division, we expressed *ftsZ1.D250A* and the equivalent *ftsZ2.D231A* mutant from plasmids in
229 their corresponding Δ*ftsZ* backgrounds. These mutants completely failed to complement the
230 division defects (Fig. 2i). The Δ*ftsZ1* + *ftsZ1.D250A* combination clearly exacerbated the
231 Δ*ftsZ1* defect (Fig. 2b-c, S13a). Similarly, Δ*ftsZ2* + *ftsZ2.D231A* displayed a mix of giant plates
232 and cell debris, but also showed filaments at the early-mid stages of culture (Fig. 2i, S13b).
233 The additional phenotypes associated with expression of the two point-mutants suggested that
234 they actively interfere with division or the cell envelope. Indeed, even moderate expression of
235 *ftsZ1.D250A* or *ftsZ2.D231A* caused strong division defects in the wild-type background (Fig.

236 S14). We therefore sought to investigate the subcellular localization and assembly of the wild-
237 type and mutant proteins.

238 ***Subcellular localization of FtsZ1 and FtsZ2***

239 Genes encoding the fluorescent proteins GFP and mCherry (mCh) were fused to the C-termini
240 of FtsZ1 and FtsZ2. FtsZ1-GFP or FtsZ1-mCh produced from plasmids (with 0.2 mM Trp)
241 partially complemented the cell division defect of the Δ*ftsZ1* strain (Fig. S15a); many cells
242 showed normal size and shape, with a fluorescent band at midcell or the division constriction,
243 whereas others were larger and occasionally misshapen with more complex fluorescent
244 structures near midcell. FtsZ2-GFP failed to complement the Δ*ftsZ2* division defect, but the
245 highly filamentous cells showed sporadic FtsZ2-GFP foci or rings that were seen ~3-4 μm from
246 a pole (Fig. S15b), suggestive of the influence of a division site positioning mechanism[28] that
247 is sensitive to pole proximity.

248 Functional interference from fluorescent proteins is very common in FtsZ and tubulin[36-38].
249 Since the FtsZ fusion proteins were not fully functional in division as the sole copy, but did
250 localize, we reasoned that they could be useful localization markers and not substantially
251 perturb cell division in the presence of the wild-type FtsZ (as seen in bacteria). Indeed, low-
252 level induction of FtsZ1 or FtsZ2 tagged with mCherry or GFP in a wild-type background did
253 not disturb normal cell size and shape. FtsZ1-mCh localized as a band at midcell or the division
254 constriction in almost all cells (Fig. 4a), with no evidence of perturbed division at 0.2 mM and
255 1 mM Trp (Fig. S15c). Similarly, FtsZ2-GFP localized at midcell or the division constriction
256 in almost all cells, which appeared normal or slightly enlarged with 0.2 mM Trp (Fig. 4b,
257 S15d). With 1 mM Trp, cells producing FtsZ2-GFP were substantially enlarged and some had
258 aberrant FtsZ2-GFP clusters near the centre, consistent with their detachment from the
259 envelope (Fig. 4b, S15d).

260 We confirmed the expected flattened ring-like structure of the midcell bands by imaging FtsZ1-
261 GFP in the wild-type background with 3D structured-illumination microscopy (Fig. 4c, upper
262 two images, ~70° xy-tilt). This also revealed patchy, discontinuous rings or short helical
263 structures (Fig. 4c, lower four images, ~20° xy tilt), similar to the appearance of bacterial Z-
264 rings[39,40]. Time-lapse imaging showed that the uneven fluorescence intensity of FtsZ1-GFP
265 around the ring was dynamic during the cell cycle (Video S9, S10) and confirmed that prompt

266 re-assembly of new rings occurs after division in orientations consistent with predictions from
267 cell morphology[28].

268 When produced together, FtsZ1-mCh and FtsZ2-GFP generally colocalized as a midcell band
269 in essentially all cells (Fig. 4d, S15e), indicating that both proteins assemble into a midcell
270 band very soon after the previous division and are maintained at midcell during cell growth.
271 Co-localization was strong, with a correlation coefficient of >0.8 in the majority of cells but
272 appeared noticeably imperfect in some (Fig. 4d). The two proteins contracted together during
273 division, which varied from bilateral to unilateral (Fig. 4) and remained generally co-localized
274 during reassembly over several cell cycles (Fig. 4d, Video S11).

275 ***Differing interdependency of FtsZ1 and FtsZ2 localization***

276 The differing functions of FtsZ1 and FtsZ2 in division, and their co-localization at midcell,
277 prompted us to investigate the dependency of FtsZ1 and FtsZ2 on each other for cellular
278 localization and assembly, by visualizing each FtsZ-FP in the alternate Δ*ftsZ* and T7-loop
279 mutant backgrounds. The T7 mutations were expected to produce aberrant hyper-stable
280 polymers and could help to resolve individual functions in divisome assembly or constriction.

281 In the absence of *ftsZ2*, FtsZ1-mCh displayed one or more clear rings (Fig. 5a) in the
282 predominantly filamentous cells (62%, Fig. S16a). The localizations were spaced on average
283 every ~5 μm, and some appeared less condensed than normal rings—as a short helicoid or
284 irregular structure (Fig. 5a, S17). Giant plate-like cells were also present (5%), which contained
285 clusters of FtsZ1-mCh (similar to that seen in Fig. 5b). In the absence of *ftsZ1*, FtsZ2-GFP
286 formed patches, foci or short filaments, but no rings (0.2 mM Trp, Fig. 5a). This strain showed
287 a much more severe division defect than Δ*ftsZ1* and Δ*ftsZ1* + unlabelled FtsZ2 (Fig. 2g-h). To
288 minimize this strong inhibitory effect of the FtsZ2-GFP, we used lower induction levels (0 or
289 50 μM Trp) and indeed observed some cells with poorly formed midcell structures, which
290 appeared as more normal rings in dividing cells (Fig. 5a, S18). Since FtsZ2-GFP induced with
291 0.2 mM Trp had only a very minor effect on division when FtsZ1 is present (Fig. 4b, S13d-e),
292 and at higher levels (1 mM Trp) it inhibited division and appeared to inhibit envelope
293 association (Fig. S15d), FtsZ1 must counteract the destabilizing effect of FtsZ2-GFP on normal
294 FtsZ2 assembly. Taken together, these results strongly suggest that FtsZ1 can assemble
295 independently of FtsZ2 and promotes and stabilizes proper FtsZ2 assembly for division at the
296 midcell envelope.

297 When FtsZ2.D231A was produced as the sole copy of FtsZ2 (in Δ*ftsZ2*) with FtsZ1-mCh,
298 highly elongated cells were observed (Fig. 5b, S16b), similar to the unlabelled strain (Fig. 2i),
299 and FtsZ1-mCh localizations again appeared as rings, broader zones or helicoid structures (Fig.
300 5b). Measurements of the FtsZ1-mCh localization intensity (compared to cellular background)
301 and individual localization thickness in the filaments (Fig. 5d) confirmed the lack of
302 condensation of some of the FtsZ1 localizations in the FtsZ2 mutants and revealed that a
303 substantially higher proportion of the total FtsZ1-mCh was localized in the absence of wild-
304 type FtsZ2. These findings suggest that FtsZ2 contributes to proper divisome condensation or
305 maturation and may limit the incorporation of FtsZ1 into the ring. In the less frequent giant
306 plates (Fig. 5b), FtsZ1-mCh showed separate filaments or diffuse clusters or only rarely as an
307 apparent ring spanning the cell, likely due to a lack of spatial cues for positioning the division
308 machinery in the giant malformed cells[28] and a low probability of assembling a ring of such
309 abnormal size. When FtsZ1.D250A was produced as the sole copy of FtsZ1 (Fig. 5b), the cells
310 formed giant plates as expected, and FtsZ2-GFP displayed patches or foci and some filaments,
311 but no rings. Overall, the moderate influence of the sole T7-mutants on the other FtsZ's
312 localization pattern, compared to the respective knockout background (Fig. 5a), suggests that
313 the sole-copy T7-mutant proteins do not efficiently homo-polymerize or do not efficiently
314 interact (or interfere) with the other FtsZ.

315 Highly informative results were obtained with the wild-type background. In this setting,
316 production of FtsZ2.D231A with FtsZ1-mCh partly inhibited division during constriction—
317 the enlarged cells often displayed one or more incomplete constrictions with FtsZ1-mCh rings
318 or occasional irregular structures present at those sites (Fig. 5c left). This strongly suggests that
319 FtsZ2.D231A mixes with wild-type FtsZ2 to inhibit GTPase-dependent constriction, and that
320 therefore the primary function of FtsZ2 and its GTPase activity is division constriction. In
321 contrast, production of FtsZ1.D250A with FtsZ2-GFP in the wild-type background caused
322 obvious aberrant filaments containing FtsZ2-GFP that were orientated seemingly at random or
323 with the longer cell axis (Fig. 5c right). Clearly, the presence of wild-type FtsZ1 in this strain
324 allows the assembly of aberrant filaments caused by FtsZ1.D250A that recruit FtsZ2-GFP
325 (compare Fig. 5a-c right), leading us to conclude that FtsZ2's subcellular localization is
326 strongly influenced by FtsZ1. Furthermore, the absence of both midcell localization and partial
327 constrictions (Fig. 5c right) indicates that the primary function of FtsZ1 and its GTPase activity
328 is the proper assembly of the division machinery.

329 To our surprise, FP-tagging of the T7-mutants—in order to simultaneously visualize both the
330 T7-mutant of one FtsZ and the wild-type copy of the other—suppressed their dominant-
331 inhibitory phenotypes (Fig. S19a-b). However, the tagged T7 mutants still partly co-localized
332 with the alternate wild-type FtsZ, and these additional experiments further confirmed the
333 relative independence of FtsZ1 filaments and the capacity of FtsZ2 to provide some structural
334 feedback in ring formation (see Supplementary Results and Discussion, and Fig. S19).

335 **Discussion**

336 We have shown that archaeal FtsZ1 and FtsZ2, from distinct families within the tubulin
337 superfamily of cytoskeletal/cytomotive proteins, both localize to the division ring but have
338 different mechanistic roles. FtsZ1 assembles largely independently of FtsZ2 and directs the
339 assembly, stabilization and correct localization of FtsZ2, whereas FtsZ2 is critical during
340 constriction, including divisome activation or structure (see Fig. 6).

341 FtsZ1 was also capable of stimulating the formation of rod and tapered morphologies from the
342 common plate/disc morphotype. *H. volcanii* rods also form during CetZ1 overproduction[20],
343 and CetZ1 can also localize at midcell or as filaments along the cell edge perpendicular to the
344 division plane during its key function in rod development. Our findings suggest a possible
345 linkage between FtsZ1 and CetZ1 function in promoting cell elongation (Fig. 6). Furthermore,
346 nascent S-layer glycoprotein (SLG) and the PssA/PssD/ArtA enzymes required for its lipid
347 modification and proper membrane anchoring were recently found to localize at midcell, and
348 blocking this pathway caused rod formation but did not affect division[41]. These findings
349 suggest a model in which FtsZ1 creates a scaffold or platform at midcell that acts as a hub or
350 landmark to recruit and stabilize the division, shape and envelope biosynthesis machineries.

351 Despite these important functions in division and shape, *H. volcanii* lacking both FtsZs could
352 be cultured indefinitely with standard solid and liquid media. FtsZ is thought to be essential for
353 division and survival in almost all walled bacteria[25], but under specific conditions of wall
354 removal ('L-forms') or excess envelope—causing cell ramification—they can produce viable
355 fragments and propagate without FtsZ[42,43]. *H. volcanii* Δ*ftsZ* strains appear similar (Fig. 2).
356 Most archaea have a lipid membrane and a flexible glycoprotein S-layer but no cell wall as in
357 peptidoglycan-enclosed bacteria[44]. Considering the morphological plasticity of wild-type *H.*
358 *volcanii*[24] and the Δ*ftsZ* strains, a turbulent liquid environment may be expected to promote
359 physical fragmentation or disintegration of the giant cells, from which any particles with a
360 complete genome may be viable and contribute to propagation without proper cytokinesis. We
361 imagine that such 'abiotic division' could have helped sustain very early life on earth. Our
362 results also suggested that budding and polar tubulation-fission might contribute to survival,
363 and similar non-FtsZ modes of proliferation can occur in wall-less bacteria[45-48]. *H. volcanii*,
364 and potentially other wall-less archaea, should therefore be suitable for studying primitive or
365 alternative division modes and the normal cellular functions underlying them.

366 While the two FtsZs are conserved in a majority of surveyed archaea (Table S3), six of the 41
367 complete genomes encode only one FtsZ each. Remarkably, we noticed that the same six
368 species, from the classes Methanobacteria and Methanopyri, are the only ones known to have
369 a pseudomurein wall analogous to bacterial peptidoglycan (murein) (Table S3)[49,50].
370 Furthermore, these classes only encode FtsZ1 homologs. The archaeal dual FtsZ system
371 therefore appears to have evolved after an early paralogous gene duplication, and then FtsZ2
372 was lost when pseudomurein evolved in those lineages.

373 In bacteria, division appears to be primarily driven by the FtsZ-directed ingrowth of the
374 peptidoglycan cell wall[3,4] and possibly an additional constriction force on the cytoplasmic
375 membrane[5,6]. Electron microscopy of Methanobacteria and Methanopyri show a clear septal
376 wall during division very similar in appearance to bacteria[51-53]. Archaea without pseudomurein
377 show a division furrow instead[54,55], and with only a single flexible S-layer (a 2D semi-
378 crystalline protein array), the archaeal envelope is almost certainly not capable of providing
379 the same directionality or structural persistence that remodelling of the covalent peptidoglycan
380 mesh would in bacterial septal ingrowth[56]. Our experimental results and the clear phylogenetic
381 association strongly suggest that FtsZ2 is required for constriction where there is no covalent
382 wall ingrowth to impose directionality to division. We therefore predict that a division complex
383 containing FtsZ2 at its core provides an intrinsic constriction force on the flexible archaeal
384 envelope. With the low or no turgor pressure in wall-less archaea, especially halophilic
385 archaea[57], this force might be sufficient to complete division[7].

386 Given the functional differentiation of two FtsZs in archaeal cell division, and the
387 corresponding lack of a cell wall, we propose that *H. volcanii* provides a powerful model for
388 mechanistic studies of cell division to contrast against the well-studied bacterial models with
389 peptidoglycan. We anticipate that this will contribute to establishing the underlying and
390 primordial principles of FtsZ-based division in all domains of life and help to unravel some of
391 the mysteries of early cellular evolution and division.

392 # Methods

393 ***Identification, phylogeny and analysis of FtsZ sequences and structure***

394 Thirteen known FtsZ protein sequences from bacteria and plants were aligned with MUSCLE[58]
395 for use as the search set to identify homologs in a diverse collection of 60 archaeal genomes
396 (Table S3) by searching their respective Reference Proteome or UniProt databases using
397 JackHMMER[59]. All significant hits were selected, excluding several redundancies and low-
398 quality sequences, and they were then aligned, together with the search set, using MUSCLE.
399 The identification of homologs belonging to either the archaeal FtsZ1, FtsZ2, CetZ, or 'other'
400 categories was done based on the position of individual sequences in a Maximum Likelihood
401 phylogenetic tree, obtained using MEGA (ver. 7.0.26)[60] with 100 bootstrap replicates, based
402 on the alignment containing only those sites with >25% occupancy. *H. volcanii* FtsZ1
403 (HVO_0717), FtsZ2 (HVO_0581) and CetZ1 (HVO_2204) were taken as the reference
404 sequences for identifying the three families.

405 To determine the percent sequence identities for each of the four domains, as defined for *H.*
406 *volcanii* FtsZ1 and FtsZ2 in Fig. S1b, the sequence alignment generated above was arranged
407 into protein families, including only those proteins classifying as FtsZ1, FtsZ2 or CetZ, and
408 was then separated into individual domain alignments using Jalview (ver. 2.9.0b2)[61]. Each set
409 was individually realigned with MUSCLE and used as input for generating a ClustalX percent
410 identity matrix[62] that was used for determining means. The crystal structure of *M. jannaschii*
411 FtsZ1[63] (PDB code: 1FSZ) was displayed with PyMol (ver. 1.7).

412 ***Growth of H. volcanii***

413 Most experimental *H. volcanii* cultures were grown in Hv-Cab medium[20] or Hv-YPC medium
414 for some genetic modification procedures[64]. Where necessary as auxotrophic requirements,
415 media were supplemented with uracil (10 µg/ml or 50 µg/ml) for Δ*pyrE2* strains, or thymidine
416 and hypoxanthine (40 µg/ml each) for Δ*hdrB* strains. Cultures were incubated at 45°C with
417 rotary shaking (200 rpm) and were generally maintained in continuous logarithmic growth
418 (OD_{600} < 0.8) for at least 2 days prior to sampling for analysis of mid-log cultures, unless
419 otherwise indicated. To control gene expression via the *p.tna* promoter, the indicated
420 concentration of L-tryptophan (Trp) (Sigma), was included in these cultures.

421 ***Genomic modification***

422 The strains used in this study and plasmids used to construct them as appropriate are listed in
423 Tables S1 and S2, respectively. In order to generate strains allowing tryptophan-controlled
424 expression of *ftsZ1* or *ftsZ2* for depletion studies (Fig. S2), two respective plasmids were first
425 constructed that can recombine with each corresponding genomic *ftsZ* locus using two-step
426 homologous recombination[64] thereby substituting the normal transcriptional regulation of *ftsZ*
427 with the specific tryptophan-inducible *p.tna* promoter. First, the upstream and downstream
428 flanks for homologous recombination on either side of each *ftsZ* gene's start codon were PCR
429 amplified from *H. volcanii* DS2 genomic DNA (upstream flank) and the corresponding
430 pIDJL40-*ftsZ* plasmid (downstream flank, containing the L11e transcription terminator and
431 *p.tna-ftsZ* cassette to be inserted), by using the primers given in Table S2. The upstream and
432 downstream fragments in each case were joined, by overlap-extension PCR, and the products
433 digested with HindIII and BamHI (sites located in the end primers; Fig. S1 and Table S2) and
434 ligated to pTA131 (at HindIII-BamHI), giving pIDJL74 (*p.tna-ftsZ1*) and pIDJL75 (*p.tna-*
435 *ftsZ2*). For *ftsZ1*, the sequence of the chosen upstream flank would result in a 39 bp deletion of
436 genomic DNA immediately upstream of the *ftsZ1* start codon during the replacement. For *ftsZ2*,
437 which is located as the second gene in a predicted operon (downstream of HVO_582, with a 2
438 bp gap), no genomic DNA was deleted when inserting the *p.tna* construct upstream of the *ftsZ2*
439 ORF. To allow direct selection of the *p.tna-ftsZ* genomic replacements, the BamHI fragment
440 from pTA1185 (T. Allers, personal communication), containing *p.fdx-hdrB*[64] was inserted at
441 the BglII site in pIDJL74 and pIDJL75 (*i.e.*, between the upstream and downstream fragments,
442 described above). Clones containing the *p.fdx-hdrB* co-directional with the downstream *p.tna-*
443 *ftsZ* cassette were selected and named pIDJL96 (*ftsZ1*) and pIDJL97 (*ftsZ2*) (Table S2).

444 Demethylated pIDJL96 and pIDJL97 (obtained via passage through *E. coli* C2925) were used
445 to transform *H. volcanii* H98 separately, selecting isolated colonies that grew on agar medium
446 (without uracil), which were expected to contain the plasmid integrated by single-crossover
447 ("pop-in")[64] between the upstream or downstream flank and the corresponding genomic *ftsZ*
448 locus. After growth of single colonies in liquid media (minus uracil), cells were plated onto
449 Hv-Ca agar containing 10 μg/mL uracil, 50 μg/mL 5-fluoroorotic acid (FOA) and 0.5 mM Trp,
450 to select for recombinational excision of these non-replicative plasmids ("pop-out")[64] that
451 following gene conversion left the cassette containing *p.fdx-hdrB* and *p.tna-ftsZ* as the only
452 copy of *ftsZ*; single colonies were streaked onto the same medium, and then arising colonies
453 were screened by allele-specific PCR to verify the expected chromosomal structure, giving
454 strains ID56 (*p.tna-ftsZ1*) and ID57 (*p.tna-ftsZ2*) (Table S1).

455 To construct plasmids for deletion of each *ftsZ* gene, PCR fragments of downstream flanking
456 DNA for *ftsZ*1 and *ftsZ2* were amplified (primers shown in Table S2). The products were
457 digested with BglII and BamHI and then ligated respectively to the large fragments of pIDJL74
458 or pIDJL75 digested with BglII, BamHI and alkaline phosphatase. Isolated clones containing
459 the appropriate co-orientation of up- and down-stream flanks were selected and named
460 pIDJL128 (*ftsZ1* flanks) and pIDJL129 (*ftsZ2* flanks) (Table S2). These plasmids were then
461 digested with BglII (*i.e.* cutting between the flanks) and then the *p.fdx-hdrB* BamHI fragment
462 from pTA1185 was ligated to them, generating pIDJL142 (for *ftsZ1* deletion) and pIDJL143
463 (for *ftsZ2* deletion).

464 To delete *ftsZ* and/or *ftsZ2* in *H. volcanii*, plasmids pIDJL142 and pIDJL143, respectively,
465 were demethylated as described above, and then used to transform *H. volcanii* H98 using the
466 two-step procedure noted above[64], yielding strains ID76 (i.e. (H98) Δ*ftsZ1-p.fdx-hdrB*), and
467 ID77 (i.e. (H98) Δ*ftsZ2-p.fdx-hdrB*). Then, to construct the double-knock-out strain, *H.*
468 *volcanii* ID77 was transformed with demethylated pIDJL128 (Table S2) using the two-step
469 method described above, generating *H. volcanii* ID112. The expected mutations were verified
470 by allele-specific PCR and genome sequencing, as described below, to detect the presence of
471 the expected *ftsZ*-deletion allele and the absence of the wild-type allele(s). In addition, the
472 expected lack of the corresponding proteins was verified with western blotting using specific
473 FtsZ1 or FtsZ2 antibodies (Fig. 1, S8d).

474 ***Genome sequencing and variant calling***

475 Whole genome sequencing libraries for strains H98, ID76, ID77 and ID112 were prepared
476 using the Illumina Nextera Flex DNA kit with custom index primers. Sequencing fragment
477 libraries were then pooled and size-selected using the SPRI-Select magnetic beads (Beckman
478 Coulter) and the pooled library was then quality checked and quantified with a Agilent
479 Bioanalyzer 2100 using the DNA HS kit (Agilent). Sequencing of was performed using an
480 Illumina MiSeq with a 300-cycle micro flow cell with V2 chemistry. Sequence data were de-
481 multiplexed using Phylosift[65] and trimmed using Trimmomatic with default settings[66]. A draft
482 H98 genome was assembled using the A5 miseq assembler (version 20150522)[67], and then the
483 trimmed reads for the three Δ*ftsZ* strains were aligned to the draft H98 genome using bwa[68].
484 Variant calling was done using bcftools mpileup and call[69]. Any single nucleotide
485 polymorphisms (SNPs) that had a quality score of less than 20 or were located within contigs
486 of less than 1000 bp were discarded. Non-synonymous variants in coding regions or any

487 variants in intergenic regions were then identified in ID76, ID77 and ID112 compared to the
488 H98 draft reference genome (Table S5).

489 ***Construction of plasmids for gene expression in H. volcanii***

490 All plasmids used are listed in Table S2. Plasmids pTA962[70] or pIDJL40 (containing GFP)[20]
491 were used as the basis to construct plasmids for controlled expression of the *ftsZ* genes or
492 modified versions. To construct pTA962-*ftsZ1*, the *ftsZ1* ORF (HVO_0717) was amplified
493 from *H. volcanii* DS70 genomic DNA using primers *ftsZ1-f* and *ftsZ-r* (Table S2), and then the
494 product was cloned between the NdeI and BamHI sites of pTA962. pTA962-*ftsZ2* was
495 constructed in the same way, except with primers *ftsZ2-f* and *ftsZ2-r* to amplify the *ftsZ2* ORF
496 (HVO_0581) (Table S2). The *ftsZ1.D250A* mutation was constructed previously[20], and the
497 *ftsZ2.D231A* mutation was similarly made by overlap extension PCR using the mutational
498 primers and primers *ftsZ2-f* and *ftsZ2-r* (Table S2) and the product cloned between NdeI and
499 BamHI in pTA962.

500 The wild-type and mutant *ftsZ* ORFs were also amplified without their stop codons ('NS'
501 primers; Table S2) and then cloned between the NdeI and BamHI sites of pIDJL40, to create
502 *ftsZ-gfp* fusions (linker encoding GS, derived from the BamHI site). Then, to construct *ftsZ1-*
503 *mCh* and *ftsZ2-mCh* fusions (pIDJL114 and pIDJL115, respectively), the GFP fragments in
504 pIDJL40-*ftsZ1* and pIDJL40-*ftsZ2* were replaced by a BamHI-NotI fragment encoding a linker
505 (GSAGSAAGSGEF, including the initial BamHI site and ending EcoRI site) and mCh (Table
506 S2), as described previously[20]. To construct plasmids for expression of the mutant *ftsZ* genes
507 tagged with mCh, NdeI + BamHI fragments (containing the point-mutant *ftsZ* genes without
508 their stop codons) were ligated to the large fragment of pIDJL117 (*i.e.* expression of *cetZ1-*
509 *mCh*) digested with NdeI and BamHI, thus replacing the *cetZ1* with the mutant *ftsZ* (Table S2).
510 The expected DNA sequences of all cloned PCR products and point mutations in this study
511 were verified by Sanger sequencing.

512 For dual expression of the various *ftsZ* genes, PvuII-fragments from the above plasmids
513 (containing a *p.tna-ftsZ* gene fusion) were ligated into HindIII-cut (Klenow blunt-ended)
514 plasmids containing the other *ftsZ* gene for the required combination, creating plasmids with
515 two independent copies of the different *p.tna-ftsZ* fusions; the combinations made are given in
516 Table S2, where the second-listed gene in the description refers to the one transferred
517 secondarily in the PvuII fragment. All plasmids were demethylated by passage through *E. coli*

518 C2925 and re-purified prior to transfer to *H. volcanii* by PEG-mediated spheroplast
519 transformation[64].

520 ***Growth curves (microtiter plate) and colony (cfu) counting***

521 Cultures maintained in log growth for at least 2 days were diluted to an OD_{600} of 0.005 with
522 fresh medium, and then 150 µL volumes were dispensed into a BD Falcon 96-well culture plate
523 per well. Absorbance (OD_{600}) of the samples over time was measured with a Tecan Spark 10M
524 microplate spectrophotometer at 42°C with an orbital shaking (amplitude 2.5 mm, 216 rpm),
525 with readings every 30 min for 56 h. Representative data from one of four independent
526 experiments were then plotted, displaying standard error bars for technical replicates of the
527 OD_{600} at each timepoint. Colony forming units (cfu) were determined by taking mid-log
528 samples of each strain at OD_{600} = 0.2, and then plating 100 µL volumes of serial dilutions onto
529 Hv-Cab (+ 50 µg/mL uracil) agar, and colonies were then counted after 4-5 days incubation in
530 a sealed bag at 45ºC.

531 ***Microscopy***

532 For transmitted light and epifluorescence microscopy, a 1 or 2 µL sample of culture was placed
533 on a 1% agarose pad containing 18% buffered saltwater (BSW) on a glass slide at room
534 temperature, and a #1.5 glass coverslip was placed on top. Images were acquired using a 1.4
535 NA oil immersion objective with phase-contrast or differential-interference contrast
536 transmission optics, or by epifluorescence with GFP (Ex: 475/28 nm; Em: 525/48 nm) or mCh
537 (Ex: 632/22 nm; Em: 676/34 nm) filter sets. 3D structured-illumination microscopy (3D-SIM)
538 was performed as previously described[20].

539 For live-cell time-lapse imaging, the 'submerged-sandwich' technique for growth of cells on
540 agarose pads[20] or a microfluidics platform were used. For agarose pads, 1-2 µL of mid-log
541 culture was placed on a ~1 mm thick gel pad (0.3% w/v agarose, containing the complete
542 medium for the required conditions), that had been prepared on an 8 mm diameter #1.5 circular
543 glass coverslip (WPI). The coverslip-pad-sample assembly was then lifted with forceps and
544 placed, inverted, onto the base of a 35 mm glass-based (#1.5) FluoroDish (WPI). Three
545 millilitres of pre-warmed liquid medium were then gently applied to cover the pad assembly
546 on the base, and the lid was applied to avoid evaporation. For microfluidics, A CellASIC ONIX
547 system was used with bacterial microfluidic plates (B04A, EMD Millipore). The flow cells
548 were first equilibrated with 1 mg/mL Bovine Serum Albumin (BSA) in phosphate-buffered
549 saline followed by 18% BSW at constant flow pressure of 5 psi. Cells were loaded into the

550 chamber and perfused with the indicated medium and pressure. Time-lapse imaging was
551 performed at 42°C or 45°C on a Nikon Ti-E microscope with a NA 1.45 oil-immersion phase-
552 contrast objective, maintaining focus automatically during time-lapse.

553 For 3D confocal imaging, live cells were stained by addition of cytoplasmic vital stain
554 Mitotracker Orange (1 μM)[71] to mid-log cultures ~18 h (45°C with shaking) prior to washing
555 the cells three times and resuspending in fresh medium (without stain), or by addition of
556 membrane dye FM1-43 (5 μg/mL) to culture samples at 45°C for 15 min. The stained cells
557 were then gently mixed with an equal volume of molten (45°C) 1% low-melting-point agarose
558 in fresh growth medium, and the mixture was placed onto the base of a FluoroDish and the
559 environment was maintained humidified with a wet tissue during imaging at 37 or 45°C. A
560 Nikon A1 laser-scanning confocal microscope was used with a 488 nm laser z-step of 0.2 μm.
561 Each 3D confocal series was deconvolved by NIS-elements software (Nikon) using blind
562 deconvolution (20 iterations). The 3D volume visualization was rendered using depth-coded
563 alpha blending to display the depth information, followed by the blind deconvolution process
564 for 20 iterations. The 3D video animations were created by rotation around Y-axis with a
565 display rate of 20 frames per second.

566 ***Image analysis***

567 To determine cell circularity, phase-contrast images were first smoothed using a Gaussian filter
568 followed by a rolling-ball background subtraction in FIJI[72]. Individual objects (cells) were then
569 identified by thresholding and filling any holes. Clearly touching cells were manually
570 separated. The minimum cell area was 0.2 μm^2 and objects overlapping the image edge were
571 excluded. The cell area was obtained from the *analyze particles* function, and cell circularity
572 was calculated by determining each cell's bounding disc coverage (the percentage area of the
573 cell within the minimal circle that completely contains the cell outline[20]) with a custom script
574 in FIJI. Cells and particles were classified as filaments (cell area > 7.5 μm^2, Circularity < 0.3),
575 giant plates (Cell area > 7.5 μm^2, Circularity > 0.3), wild-type-like cells (any shape, with cell
576 area between 1.5 μm^2 and 7.5 μm^2), or cellular debris (< 1.5 μm^2), as indicated in the graphs.

577 FtsZ1 and FtsZ2 medial localization along the cell long axis (Fig. 4) was then done with FIJI[72]
578 and MicrobeJ[73]. Fluorescent images were pre-treated with the background subtraction filter
579 (ballsize = 8) in FIJI. Cell outlines were detected in MicrobeJ by phase-contrast image
580 segmentation using the Otsu method, with medial axis mode, area >0.98, and exclude-on-edges
581 options, and then manually corrected where needed. FtsZ foci were detected using the 'Foci'

582 and 'Smoothed' modes with a tolerance of 160, a Z-score of 8, and area >0.005. Raw pixel
583 intensities and medial profiles were recorded. Data were output using the MicrobeJ
584 XStatProfile Plot function with the parameters: Stat: Median, Y axis: MEDIAL.intensity.ch1
585 (and 2 for colocalization), bin#:150. The correlation coefficients for individual cells for FtsZ1
586 and FtsZ2 fluorescence were obtained using the MicrobeJ statistics functions, Stat.: count,
587 Data: EXPERIMENT.count.total. Split horizontal: INTENSITY.ch2.correlation.ch1.

588 To determine FtsZ1-mCh localization frequency, intensity and thickness (Fig. 5, S17), cell
589 outlines (regions of interest, ROIs) were first obtained from the phase-contrast channel in FIJI,
590 by combining automated detection and manual curation. The long medial axis for each cell was
591 then identified and the fluorescence channel data (after image/sensor background subtraction)
592 were then quantified by averaging the intensity on the transverse axis to create a longitudinal
593 intensity profile. Gaussian peaks were fitted to the significant localizations and a spline fit to
594 the cellular Z1-mCh fluorescence background. The localization thickness was taken as the
595 width of the fitted Gaussian peaks at half height (μm), and the intensity was taken as the
596 integrated peak area (per μm across the cell).

597 ***Coulter and flow cytometry***

598 For Coulter cytometry to obtain cell volume distributions, culture samples were diluted (1:100
599 or 1:1000) with 0.2-μm-filtered 18% BSW and were analysed with a Multisizer M4 Coulter
600 cytometer (Beckman-Coulter) equipped with a 20 or 30 μm aperture tube, running and
601 calibrated with 2 μm latex beads in 18% BSW as the electrolyte. Runs were completed in the
602 volumetric mode (100 μL), with a current of 600 μA and gain of 4. For flow cytometry, mid-
603 log culture samples were diluted 1:10 with a solution of 5 μM SYTOX Green in 18% BSW
604 and incubated at room temperature for ~30 min before log-scale data acquisition (triggered by
605 a side-scatter threshold) with an LSR-II flow cytometer (BD) with 18% BSW as sheath fluid.
606 Cell sampling size normally ranged between 30,000 to 100,000 events per sample.

607 ***Western blotting***

608 Rabbit antisera for detection of *H. volcanii* FtsZ1 and FtsZ2 were generated with a synthetic
609 peptide antigen derived from the sequence of the C-terminal region of FtsZ1,
610 (QAHAEERLEDIDYVE, Cambridge Research Biochemicals, UK), used at 1:1000 dilution of
611 serum. For FtsZ2, antibodies were raised against a peptide containing an N-terminally derived
612 sequence (ERQTQSSLEDSDDQFGDPR, Thermo Fisher, USA) (1:500 dilution of serum), and
613 one derived from the C-terminal region (SDGGRDEVEKNNGLDVIR, Thermo Fisher, USA)

614 (1:4000 dilution of affinity purified antibody stock of 2.95 mg/ml). The FtsZ2 antibodies were
615 used either as diluted serum or affinity purified protein (selecting for binding for the target
616 peptide), as follows. N-term (serum): Fig. 1b, S6c, S8d, and C-term (affinity purified): Fig. 3d.

617 *H. volcanii* cell pellets (carefully separated from any excess liquid medium) were resuspended
618 in SDS–PAGE sample buffer and then the samples were heated (95°C, 5 min) and vortexed.
619 Samples were separated by SDS-PAGE, and then electroblotted (Bio-Rad) on a nitrocellulose
620 membrane (Protran, Whatman), and probed with the rabbit polyclonal primary antibodies
621 described above, followed by secondary antibody (donkey anti-rabbit IgG-HRP, AbCam
622 16284, 1:5000 dilution), with standard techniques. Bands were detected by enhanced
623 chemiluminescence reagents (Thermo Fisher) with an Amersham Imager 600 system.

624 ***Experimental replication and data and materials availability***

625 In addition to the preliminary experiments carried out throughout this study, the data displayed
626 are representative of at least two biological replicate experiments, and the displayed
627 microscopy images and accompanying descriptions were selected to fairly represent the whole
628 sample dataset, which was quantitatively analysed as described and represented in full. The
629 data and biological materials that support the findings of this study are available from the
630 corresponding author upon reasonable request. Genome sequence data has been deposited at
631 NCBI under BioProject PRJNA681931.

632

633 **Acknowledgments**

634 This study was supported by the Australian Research Council (FT160100010 to IGD) and the
635 UK Biotechnology and Biological Sciences Research Council (BBSRC) and Medical Research
636 Council (U105184326 to JL). For technical support, we thank Lynne Turnbull, Michael
637 Johnson and Louise Cole from the UTS Microbial Imaging Facility (MIF), and Kay
638 Anantanawat and Michael Liu from the UTS DNA sequencing facility.

639 **Author Contributions**

640 Designed research: ID, SI, YL, JL. Preliminary data and strain construction: ID, SI, YL.
641 Contributed/analysed data: Fig. 1: YL, Fig. 2: YL (b-i), SI (a), Fig. 3: YL, Fig. 4: SI (a, b, d),
642 ID (c), Fig. 5: SI (a-d), YL/ID (a), CE (d), Fig. 6: SI/YL/ID. Supplementary Figures: S1: ID,
643 S2: YL/ID, S3: YL, S4: YL, S5: ID, S6: YL, S7: YL/CE, S8: YL, S9: YL , S10: YL, S12: YL,
644 S13: YL, S14: SI, S15: SI, S16: SI/CE, S17: CE/SI/ID, S18: YL/SI, S19: SI. Supplementary
645 Tables: S1: ID/SI, S2: ID/SI, S3: ID, S4: ID, S5: YL, S6: SI/YL. Supplementary Videos: S1-
646 S8: YL, S9-S10: ID/YL, S11: SI. Interpreted results, wrote and reviewed the manuscript and
647 figures: ID, YL/SI, JL, CE. Management, funding acquisition and supervision: ID, JL.

648 **Declaration of Interests**

649 The authors declare no competing interests.

650 **Supplementary Information**

651 Supplementary videos, and a file containing supplementary results and discussion, tables,
652 figures, video legends and references are available with the online version of this article.
653 Genome sequence data has been deposited at NCBI under BioProject PRJNA681931.

654 **References**

655 1. Adams, D.W. & Errington, J. Bacterial cell division: assembly, maintenance and
656 disassembly of the Z ring. *Nat Rev Microbiol* **7**, 642-653 (2009).
657 2. Du, S. & Lutkenhaus, J. Assembly and activation of the *Escherichia coli* divisome.
658 *Mol Microbiol* **105**, 177-187 (2017).
659 3. Bisson-Filho, A.W. et al. Treadmilling by FtsZ filaments drives peptidoglycan
660 synthesis and bacterial cell division. *Science* **355**, 739-743 (2017).
661 4. Yang, X. et al. GTPase activity-coupled treadmilling of the bacterial tubulin FtsZ
662 organizes septal cell wall synthesis. *Science* **355**, 744-747 (2017).
663 5. Osawa, M., Anderson, D.E. & Erickson, H.P. Reconstitution of contractile FtsZ rings
664 in liposomes. *Science* **320**, 792-794 (2008).
665 6. Szwedziak, P., Wang, Q., Bharat, T.A., Tsim, M. & Lowe, J. Architecture of the ring
666 formed by the tubulin homologue FtsZ in bacterial cell division. *Elife* **3**, e04601
667 (2014).
668 7. Osawa, M. & Erickson, H.P. Turgor Pressure and Possible Constriction Mechanisms
669 in Bacterial Division. *Front Microbiol* **9**, 111 (2018).
670 8. Zhou, X. et al. Bacterial division. Mechanical crack propagation drives millisecond
671 daughter cell separation in *Staphylococcus aureus*. *Science* **348**, 574-578 (2015).
672 9. Typas, A., Banzhaf, M., Gross, C.A. & Vollmer, W. From the regulation of
673 peptidoglycan synthesis to bacterial growth and morphology. *Nat Rev Microbiol* **10**,
674 123-136 (2012).
675 10. Margolin, W., Wang, R. & Kumar, M. Isolation of an *ftsZ* homolog from the
676 archaebacterium *Halobacterium salinarium*: implications for the evolution of FtsZ
677 and tubulin. *J Bacteriol* **178**, 1320-1327 (1996).
678 11. Wang, X. & Lutkenhaus, J. FtsZ ring: the eubacterial division apparatus conserved in
679 archaebacteria. *Mol Microbiol* **21**, 313-319 (1996).
680 12. Baumann, P. & Jackson, S.P. An archaebacterial homologue of the essential
681 eubacterial cell division protein FtsZ. *Proceedings of the National Academy of*
682 *Sciences of the United States of America* **93**, 6726-6730 (1996).
683 13. Poplawski, A., Gullbrand, B. & Bernander, R. The *ftsZ* gene of *Haloferax*
684 *mediterranei*: sequence, conserved gene order, and visualization of the FtsZ ring.
685 *Gene* **242**, 357-367 (2000).
686 14. Krupka, M. & Margolin, W. Unite to divide: Oligomerization of tubulin and actin
687 homologs regulates initiation of bacterial cell division. *F1000Res* **7**, 235 (2018).
688 15. Duman, R. et al. Structural and genetic analyses reveal the protein SepF as a new
689 membrane anchor for the Z ring. *Proc Natl Acad Sci U S A* **110**, E4601-4610 (2013).
690 16. Makarova, K.S. & Koonin, E.V. Two new families of the FtsZ-tubulin protein
691 superfamily implicated in membrane remodeling in diverse bacteria and archaea. *Biol*
692 *Direct* **5**, 33 (2010).
693 17. Bult, C.J. et al. Complete genome sequence of the methanogenic archaeon,
694 *Methanococcus jannaschii*. *Science* **273**, 1058-1073 (1996).
695 18. Lindas, A.C., Karlsson, E.A., Lindgren, M.T., Ettema, T.J. & Bernander, R. A unique
696 cell division machinery in the Archaea. *Proceedings of the national academy of*
697 *sciences of the United States of America* **105**, 18942-18946 (2008).
698 19. Samson, R.Y., Obita, T., Freund, S.M., Williams, R.L. & Bell, S.D. A role for the
699 ESCRT system in cell division in archaea. *Science* **322**, 1710-1713 (2008).
700 20. Duggin, I.G. et al. CetZ tubulin-like proteins control archaeal cell shape. *Nature* **519**,
701 362-365 (2015).

702 21. Aylett, C.H.S. & Duggin, I.G. The tubulin superfamily in archaea. *Subcellular*
703 *Biochemistry* **84**, 393-417 (2017).
704 22. Hartman, A.L. et al. The complete genome sequence of *Haloferax volcanii* DS2, a
705 model archaeon. *PLoS One* **5**, e9605 (2010).
706 23. Bisson-Filho, A.W., Zheng, J. & Garner, E. Archaeal imaging: leading the hunt for
707 new discoveries. *Molecular biology of the cell* **29**, 1675-1681 (2018).
708 24. de Silva, R.T. et al. Improved growth and morphological plasticity of *Haloferax*
709 *volcanii*. *Microbiology* **In Press** (2021).
710 25. Erickson, H.P. & Osawa, M. Cell division without FtsZ--a variety of redundant
711 mechanisms. *Mol Microbiol* **78**, 267-270 (2010).
712 26. Large, A. et al. Characterization of a tightly controlled promoter of the halophilic
713 archaeon *Haloferax volcanii* and its use in the analysis of the essential *cct1* gene. *Mol*
714 *Microbiol* **66**, 1092-1106 (2007).
715 27. Slater, M. & Schaechter, M. Control of cell division in bacteria. *Bacteriol Rev* **38**,
716 199-221 (1974).
717 28. Walsh, J.C. et al. Division plane placement in pleomorphic archaea is dynamically
718 coupled to cell shape. *Mol Microbiol* **112**, 785-799 (2019).
719 29. Breuert, S., Allers, T., Spohn, G. & Soppa, J. Regulated polyploidy in halophilic
720 archaea. *PLoS One* **1**, e92 (2006).
721 30. Delmas, S., Duggin, I.G. & Allers, T. DNA damage induces nucleoid compaction via
722 the Mre11-Rad50 complex in the archaeon *Haloferax volcanii*. *Molecular*
723 *Microbiology* **87**, 168-179 (2013).
724 31. Coltharp, C. & Xiao, J. Beyond force generation: Why is a dynamic ring of FtsZ
725 polymers essential for bacterial cytokinesis? *Bioessays* **39**, 1-11 (2017).
726 32. Nogales, E., Downing, K.H., Amos, L.A. & Lowe, J. Tubulin and FtsZ form a distinct
727 family of GTPases. *Nature Structural Biology* **5**, 451-458 (1998).
728 33. Chen, Y., Bjornson, K., Redick, S.D. & Erickson, H.P. A rapid fluorescence assay for
729 FtsZ assembly indicates cooperative assembly with a dimer nucleus. *Biophys J* **88**,
730 505-514 (2005).
731 34. Scheffers, D.J., de Wit, J.G., den Blaauwen, T. & Driessen, A.J. GTP hydrolysis of
732 cell division protein FtsZ: evidence that the active site is formed by the association of
733 monomers. *Biochemistry* **41**, 521-529 (2002).
734 35. Scheffers, D.J., de Wit, J.G., den Blaauwen, T. & Driessen, A.J. Substitution of a
735 conserved aspartate allows cation-induced polymerization of FtsZ. *FEBS Lett* **494**,
736 34-37 (2001).
737 36. Kimble, M., Kuzmiak, C., McGovern, K.N. & de Hostos, E.L. Microtubule
738 organization and the effects of GFP-tubulin expression in *Dictyostelium discoideum*.
739 *Cell Motil Cytoskeleton* **47**, 48-62 (2000).
740 37. Moore, D.A., Whatley, Z.N., Joshi, C.P., Osawa, M. & Erickson, H.P. Probing for
741 Binding Regions of the FtsZ Protein Surface through Site-Directed Insertions:
742 Discovery of Fully Functional FtsZ-Fluorescent Proteins. *J Bacteriol* **199** (2017).
743 38. Sun, Q. & Margolin, W. FtsZ dynamics during the division cycle of live *Escherichia*
744 *coli* cells. *J Bacteriol* **180**, 2050-2056 (1998).
745 39. Rowlett, V.W. & Margolin, W. 3D-SIM super-resolution of FtsZ and its membrane
746 tethers in Escherichia coli cells. *Biophys J* **107**, L17-L20 (2014).
747 40. Strauss, M.P. et al. 3D-SIM super resolution microscopy reveals a bead-like
748 arrangement for FtsZ and the division machinery: implications for triggering
749 cytokinesis. *PLoS Biol* **10**, e1001389 (2012).
750 41. Abdul-Halim, M.F. et al. Lipid Anchoring of Archaeosortase Substrates and Midcell
751 Growth in Haloarchaea. *mBio* **11** (2020).

752 42. Leaver, M., Dominguez-Cuevas, P., Coxhead, J.M., Daniel, R.A. & Errington, J. Life
753 without a wall or division machine in *Bacillus subtilis*. *Nature* **457**, 849-853 (2009).
754 43. Mercier, R., Kawai, Y. & Errington, J. Wall proficient *E. coli* capable of sustained
755 growth in the absence of the Z-ring division machine. *Nat Microbiol* **1**, 16091 (2016).
756 44. Albers, S.V. & Meyer, B.H. The archaeal cell envelope. *Nat Rev Microbiol* **9**, 414-
757 426 (2011).
758 45. Abdelrahman, Y., Ouellette, S.P., Belland, R.J. & Cox, J.V. Polarized Cell Division
759 of *Chlamydia trachomatis*. *PLoS pathogens* **12**, e1005822 (2016).
760 46. Errington, J. L-form bacteria, cell walls and the origins of life. *Open Biol* **3**, 120143
761 (2013).
762 47. Lluch-Senar, M., Querol, E. & Pinol, J. Cell division in a minimal bacterium in the
763 absence of ftsZ. *Mol Microbiol* **78**, 278-289 (2010).
764 48. Rivas-Marin, E. et al. Non-essentiality of canonical cell division genes in the
765 planctomycete *Planctopirus limnophila*. *Sci Rep* **10**, 66 (2020).
766 49. Steenbakkers, P.J., Geerts, W.J., Ayman-Oz, N.A. & Keltjens, J.T. Identification of
767 pseudomurein cell wall binding domains. *Mol Microbiol* **62**, 1618-1630 (2006).
768 50. Visweswaran, G.R., Dijkstra, B.W. & Kok, J. Murein and pseudomurein cell wall
769 binding domains of bacteria and archaea--a comparative view. *Appl Microbiol*
770 *Biotechnol* **92**, 921-928 (2011).
771 51. Burggraf, S., Stetter, K.O., Rouviere, P. & Woese, C.R. *Methanopyrus kandleri*: an
772 archaeal methanogen unrelated to all other known methanogens. *Syst Appl Microbiol*
773 **14**, 346-351 (1991).
774 52. Zeikus, J.G. The biology of methanogenic bacteria. *Bacteriol Rev* **41**, 514-541 (1977).
775 53. Zeikus, J.G. & Wolfe, R.S. Fine structure of *Methanobacterium*
776 *thermoautotrophicum*: effect of growth temperature on morphology and
777 ultrastructure. *J Bacteriol* **113**, 461-467 (1973).
778 54. Dobro, M.J. et al. Electron cryotomography of ESCRT assemblies and dividing
779 *Sulfolobus* cells suggests that spiraling filaments are involved in membrane scission.
780 *Molecular biology of the cell* **24**, 2319-2327 (2013).
781 55. Mullakhanbhai, M.F. & Larsen, H. *Halobacterium volcanii spec. nov.*, a Dead Sea
782 halobacterium with a moderate salt requirement. *Arch Microbiol* **104**, 207-214 (1975).
783 56. Liao, Y., Ithurbide, S., de Silva, R.T., Erdmann, S. & Duggin, I.G. Archaeal cell
784 biology: diverse functions of tubulin-like cytoskeletal proteins at the cell envelope.
785 *Emerg Top Life Sci* **2**, 547-559 (2018).
786 57. Walsby, A.E. & Fogg, G.E. The pressure relationships of gas vacuoles. *Proceedings*
787 *of the Royal Society of London. Series B. Biological Sciences* **178**, 301-326 (1971).
788 58. Edgar, R.C. MUSCLE: multiple sequence alignment with high accuracy and high
789 throughput. *Nucleic acids res* **32**, 1792-1797 (2004).
790 59. Potter, S.C. et al. HMMER web server: 2018 update. *Nucl Acids Res* **46**, W200-W204
791 (2018).
792 60. Kumar, S., Stecher, G., Li, M., Knyaz, C. & Tamura, K. MEGA X: Molecular
793 Evolutionary Genetics Analysis across Computing Platforms. *Mol Biol Evol* **35**, 1547-
794 1549 (2018).
795 61. Waterhouse, A.M., Procter, J.B., Martin, D.M., Clamp, M. & Barton, G.J. Jalview
796 Version 2--a multiple sequence alignment editor and analysis workbench.
797 *Bioinformatics* **25**, 1189-1191 (2009).
798 62. Thompson, J.D., Gibson, T.J. & Higgins, D.G. Multiple sequence alignment using
799 ClustalW and ClustalX. *Current protocols in bioinformatics / editoral board, Andreas*
800 *D. Baxevanis ... [et al.]* **Chapter 2**, Unit 2 3 (2002).

801 63. Löwe, J. Crystal structure determination of FtsZ from Methanococcus jannaschii. *J*
802 *Struct Biol* **124**, 235-243 (1998).
803 64. Allers, T., Ngo, H.P., Mevarech, M. & Lloyd, R.G. Development of additional
804 selectable markers for the halophilic archaeon *Haloferax volcanii* based on the *leuB*
805 and *trpA* genes. *Appl Environ Microbiol* **70**, 943-953 (2004).
806 65. Darling, A.E. et al. PhyloSift: phylogenetic analysis of genomes and metagenomes.
807 *PeerJ* **2**, e243 (2014).
808 66. Bolger, A.M., Lohse, M. & Usadel, B. Trimmomatic: a flexible trimmer for Illumina
809 sequence data. *Bioinformatics* **30**, 2114-2120 (2014).
810 67. Coil, D., Jospin, G. & Darling, A.E. A5-miseq: an updated pipeline to assemble
811 microbial genomes from Illumina MiSeq data. *Bioinformatics* **31**, 587-589 (2015).
812 68. Li, H. & Durbin, R. Fast and accurate short read alignment with Burrows-Wheeler
813 transform. *Bioinformatics* **25**, 1754-1760 (2009).
814 69. Li, H. et al. The Sequence Alignment/Map format and SAMtools. *Bioinformatics* **25**,
815 2078-2079 (2009).
816 70. Allers, T., Barak, S., Liddell, S., Wardell, K. & Mevarech, M. Improved strains and
817 plasmid vectors for conditional overexpression of His-tagged proteins in *Haloferax*
818 *volcanii*. *Appl Environ Microbiol* **76**, 1759-1769 (2010).
819 71. Maslov, I. et al. Efficient non-cytotoxic fluorescent staining of halophiles. *Sci Rep* **8**,
820 2549 (2018).
821 72. Schindelin, J. et al. Fiji: an open-source platform for biological-image analysis.
822 *Nature methods* **9**, 676-682 (2012).
823 73. Ducret, A., Quardokus, E.M. & Brun, Y.V. MicrobeJ, a tool for high throughput
824 bacterial cell detection and quantitative analysis. *Nat Microbiol* **1**, 16077 (2016).

825

826 **Figures**

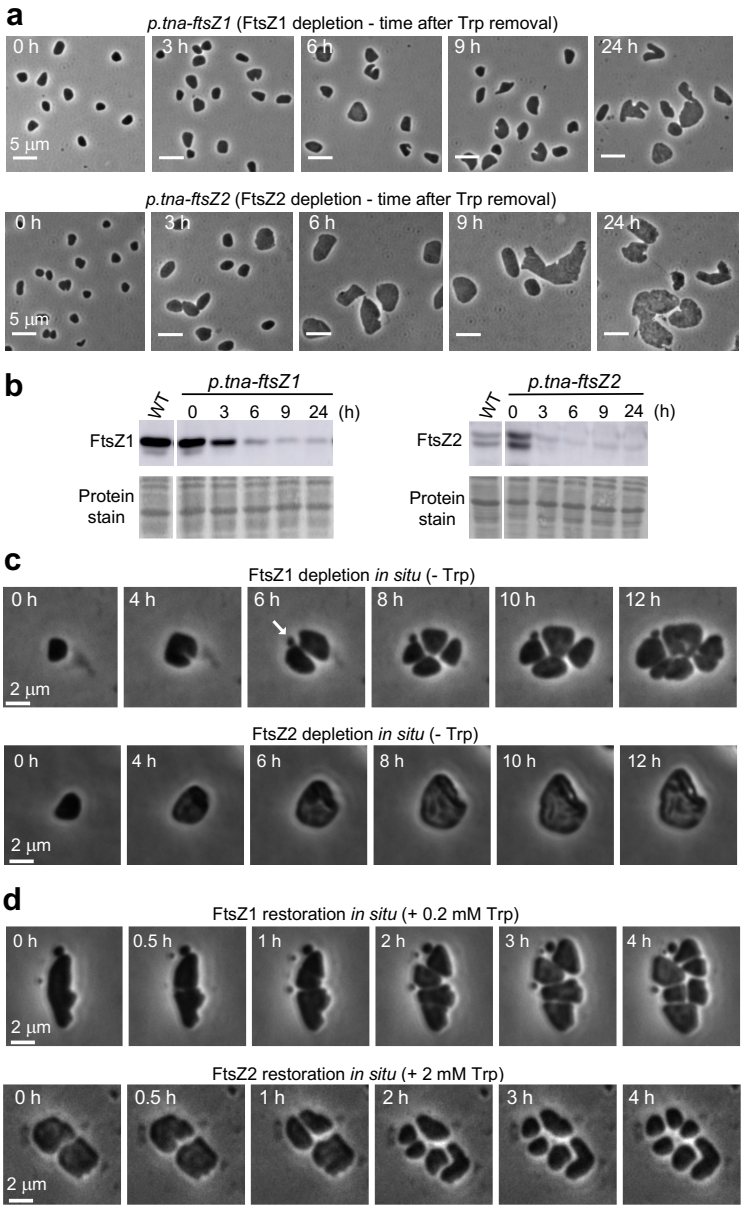

827

828 **Figure 1. Depletion of FtsZ1 or FtsZ2 results in defects in cell division.** (a) Phase-contrast
829 microscopy of samples from cultures (*H. volcanii* ID56 - *p.tna-ftsZ1*, and ID57 - *p.tna-ftsZ2*)
830 immediately prior to (0 h) or at the indicated time-points after resuspension of cells (to OD_{600}
831 = 0.25) in growth medium without Trp. (b) Western blots probed with FtsZ1 or FtsZ2 antisera
832 during depletion with the corresponding Ponceau S pre-staining of total protein. The separate
833 wild-type (H26) panels were from the same blots for each protein; FtsZ1 (~40 kDa) and FtsZ2
834 (~43 kDa) bands are indicated. The double band for FtsZ2 suggests a modified/clipped form.
835 (c) *In situ* time-lapse imaging of FtsZ depletion. Cells cultured in Hv-Cab + 2 mM Trp were
836 washed and placed onto agarose media pads without Trp and imaged over time. Morphology
837 of giant cells differs from the liquid culture (a), most likely due to the support provided by
838 growth on agarose. (d) *In situ* time-lapse imaging of FtsZ restoration. The respective *p.tna-ftsZ*
839 strains were initially grown for ~2 days without Trp inducer, and then cells were washed and
840 placed onto agarose media (Hv-Cab) pads including 0.2 mM Trp for FtsZ1, and 2 mM Trp for
841 FtsZ2. Scale bars (c-d), 2 µm.

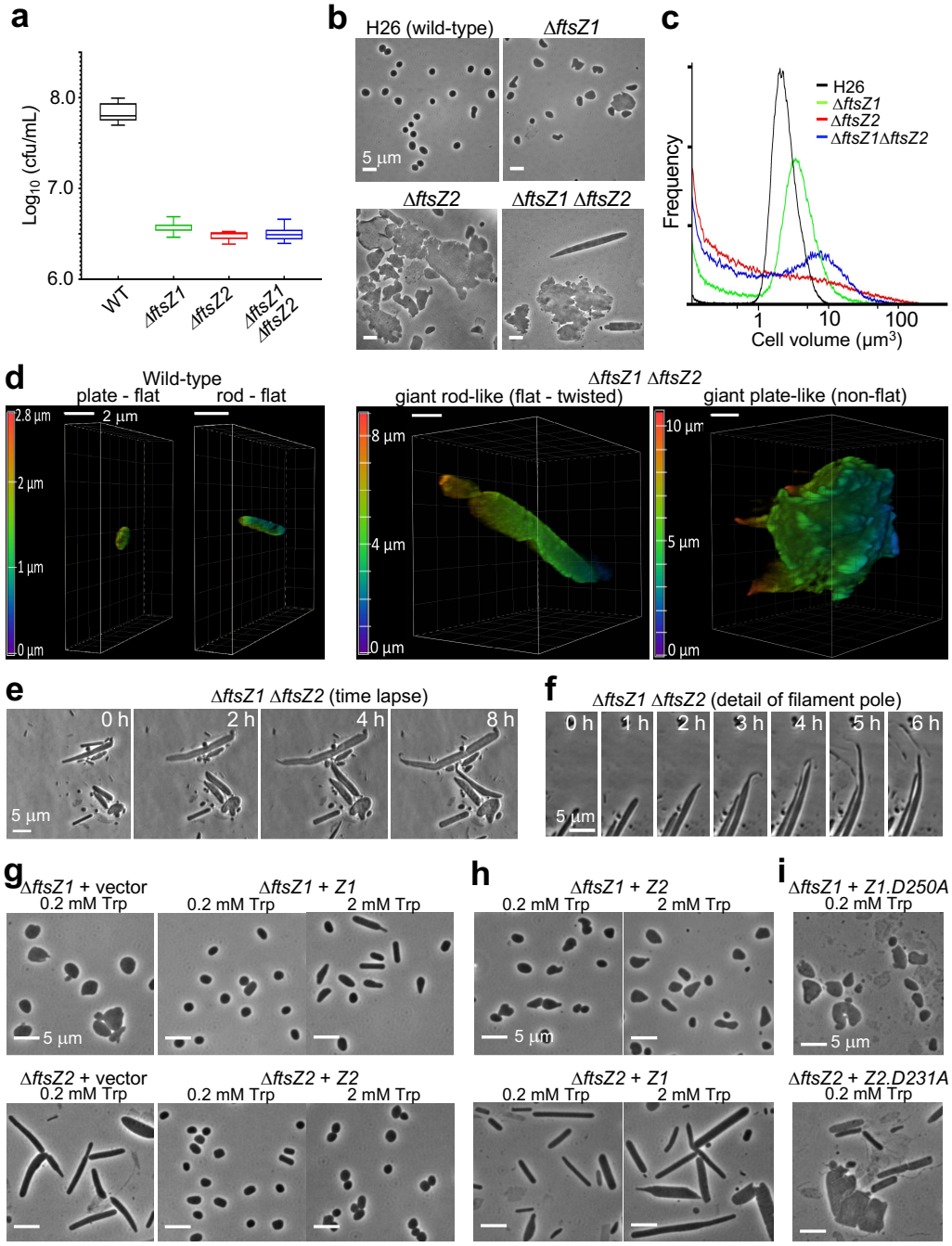

Figure 2. FtsZ1 and FtsZ2 are dispensable for survival but required for normal cell division. (a) Box-and-whisker plots of agar colony counts (cfu/mL) of *H. volcanii* wild-type (H26), Δ*ftsZ1* (ID76), Δ*ftsZ2* (ID77), and Δ*ftsZ1* Δ*ftsZ2* (ID112), sampled during mid-log growth (OD_{600} = 0.2) in Hv-Cab medium (+ 50 µg/mL uracil) (n = 4 separate cultures). (b) Phase-contrast images and (c) Coulter cell-volume frequency distributions (normalized to total count). (d) Confocal microscopy 3D-reconstructed images of cells stained with Mitotracker Orange and embedded in low melting point agarose. The reconstructions are shown with a ~45º rotation around the x-axis. The colour scale indicates the z-depth. Similar morphologies were seen with other *ftsZ* mutants and FM1-43 membrane staining (Fig. S7b). (e) Live cell time-lapse images of the Δ*ftsZ1* Δ*ftsZ2* strain growing on an agarose gel media pad, and (f) showing polar tubulation and budding-like processes. (g-i) Phase-contrast microscopy of *H. volcanii* strains containing expression plasmids, as indicated, sampled in steady mid-log growth in Hv-Cab medium with the indicated concentrations of Trp.

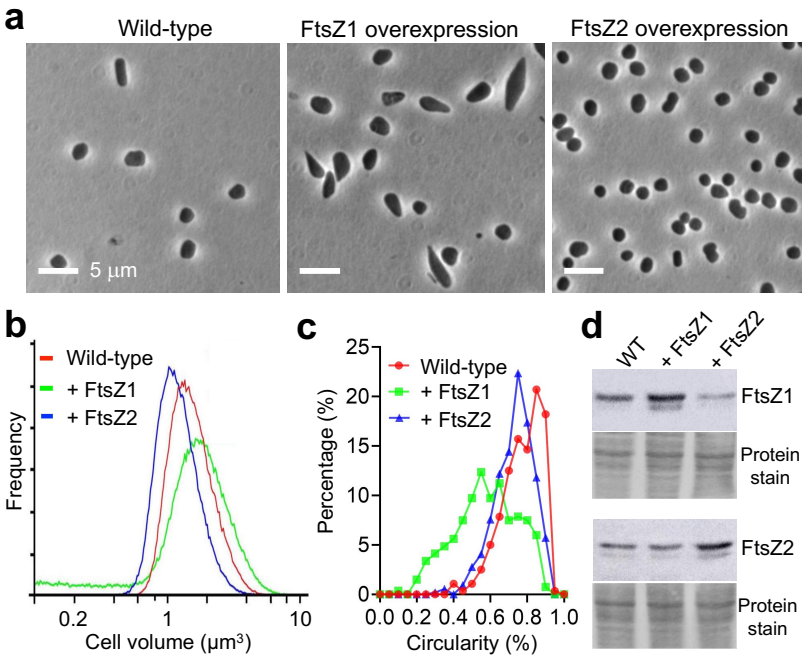

Figure 3. Overproduction of FtsZ1 or FtsZ2 differentially affects cell division and shape. (a) Phase contrast micrographs of *H. volcanii* wild-type (H98 + pTA962), ID25 (FtsZ1 overproduction, H98 + pTA962-*ftsZ1*) and ID26 (FtsZ2 overproduction strain, H98 + pTA962-*ftsZ2*) during steady mid-log cultures in Hv-Cab + 2 mM Trp. Scale bars, 5 µm. (b) Coulter cell-volume frequency distributions (normalized to total count) of the strains in panel (a). (c) Frequency distributions of the circularity of cell outlines (WT, n = 280; + FtsZ1, n = 267; + FtsZ2, n = 534). (d) Western blots of whole cell lysates of the wild-type, FtsZ1 overproduction and FtsZ2 overproduction strains, probed with FtsZ1 or FtsZ2 antisera, as indicated. Total protein pre-staining of each membrane (with Ponceau S) is shown as a loading control.

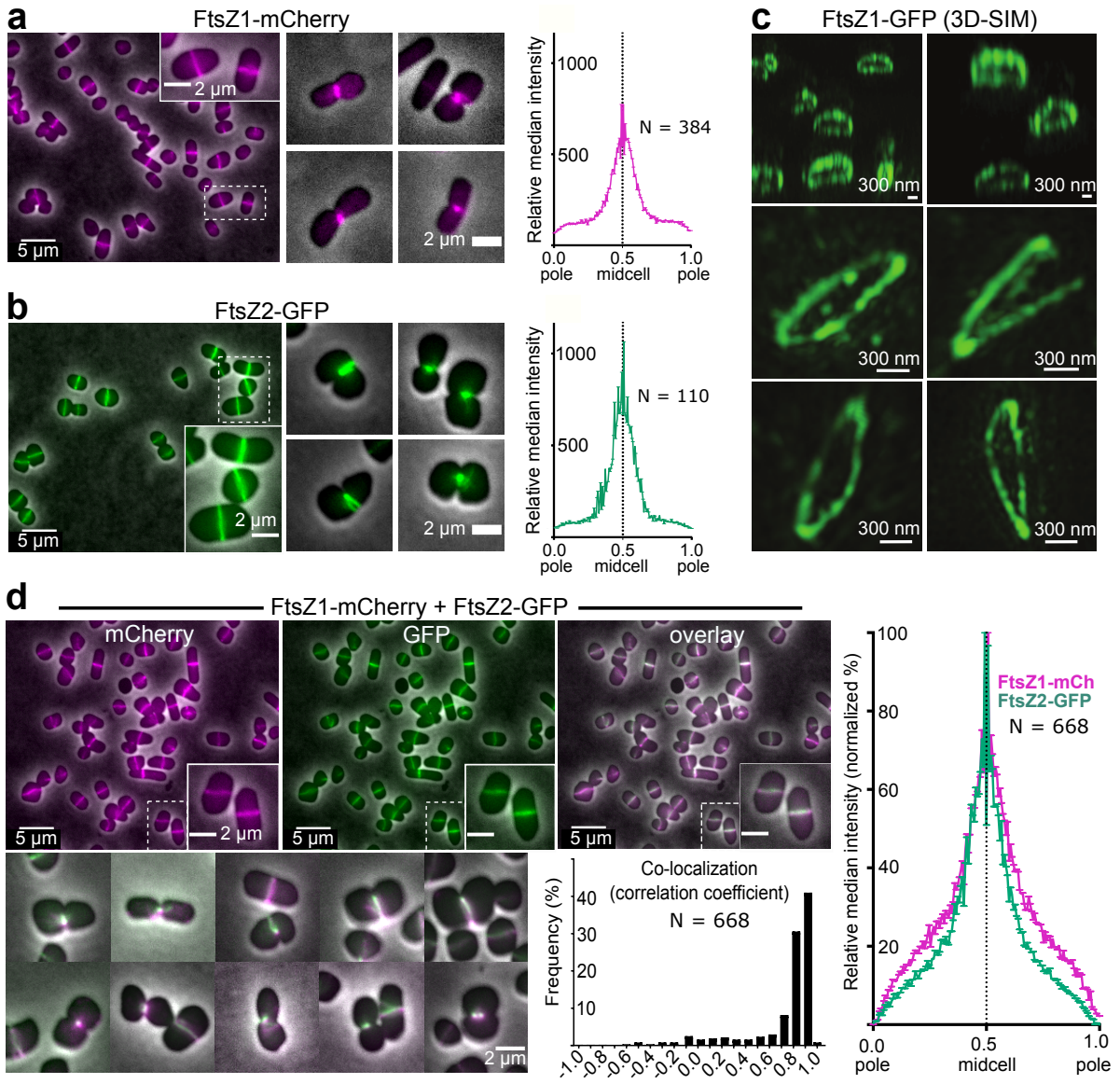

Figure 4. Midcell localization of FtsZ1-mCh and FtsZ2-GFP. Mid-log cultures of (a) *H. volcanii* ID49 (WT + FtsZ1-mCh), (b) ID17 (WT + FtsZ2-GFP) and (d) ID67 (WT + FtsZ1-mCh + FtsZ2-GFP dual localization), cultured with 0.2 mM Trp, were imaged by phase-contrast and fluorescence microscopy. The mCh (magenta) and GFP (green) fluorescence was quantified along the long axis of cells, by plotting the relative (normalized) median intensity perpendicular to the long axis. (c) 3D-SIM images of *H. volcanii* ID16 (WT + FtsZ1-GFP) sampled during mid-log growth with 0.2 mM Trp. The upper two panels show a 'side-on' view (~70° tilt of the xy view), and the lower four panels show a ~20° xy tilt. (d) Co-localization of FtsZ1-mCh and FtsZ2-GFP fluorescence in cells, including selected examples of dividing cells (lower left). Correlation coefficients were plotted as a frequency distribution (80% of the cells had a correlation coefficient greater or equal to 0.7). The ring containing FtsZ1 and FtsZ2 closes down with division constrictions that range between unilateral to partially and equally bilateral.

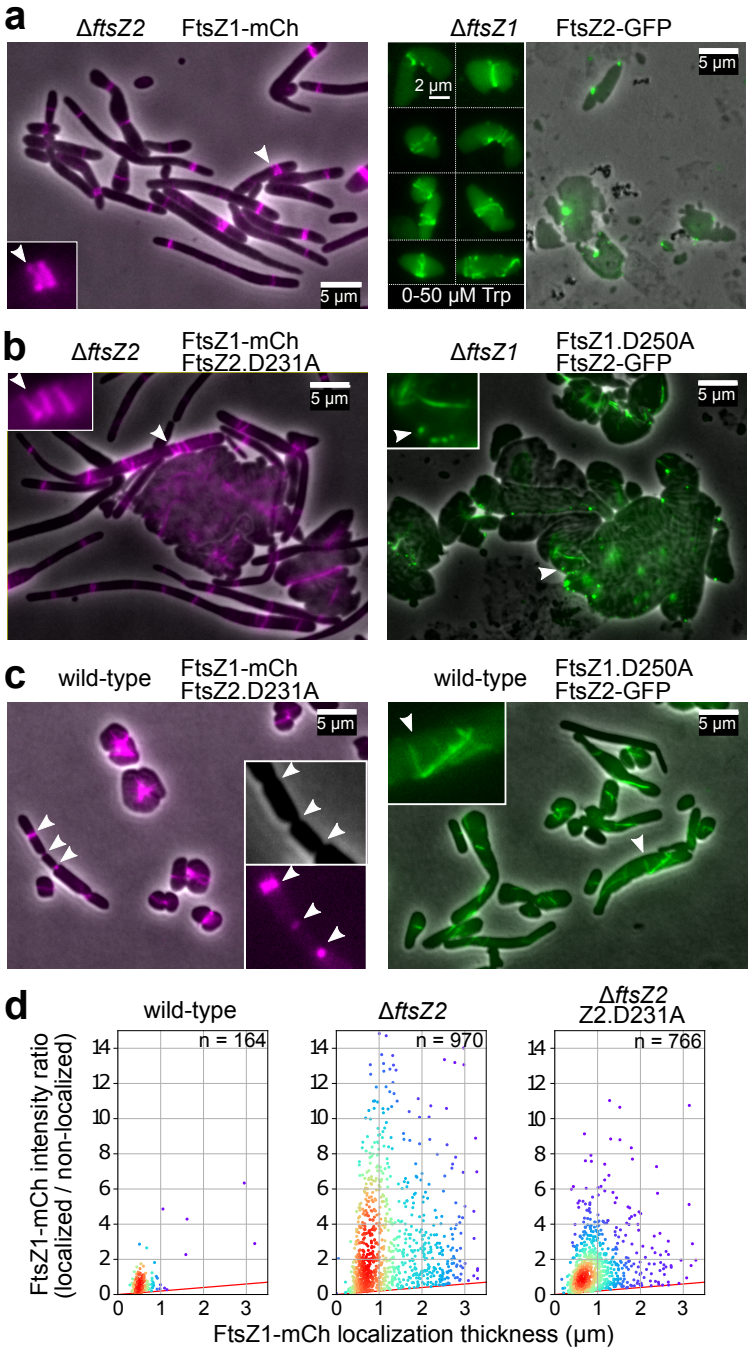

Figure 5. Localization interdependency and the effect of FtsZ mutations on FtsZ1-mCh and FtsZ2-GFP localization. Fluorescence and phase-contrast microscopy of mid-log *H. volcanii* strains (wild-type or Δ*ftsZ* backgrounds) carrying plasmid copies of the indicated *ftsZ* mutants and fusion proteins. Strains were grown with 0.2 mM Trp unless otherwise specified. Insets show either a magnified view at the arrowhead in the main panels, or represent another culture grown with the indicated concentration of Trp. (a) Localization of each FtsZ in the absence of the other FtsZ. (b) Localization of each FtsZ in the presence of the T7-loop mutant as the sole copy of the other. (c) Localization of each FtsZ in the wild-type genomic background expressing the T7-loop mutant of the other. Inset scale bars are 5 µm unless indicated otherwise. (d) Plots of FtsZ1-mCh localization relative intensity (per µm across the cell, as a ratio over the mean cellular background FtsZ1-mCh fluorescence) *versus* localization thickness (µm) in the indicated strain backgrounds. Data-points are coloured with a proximity heatmap. Representative images of the wild-type background can be seen in Fig 4a. See also Fig. S17.

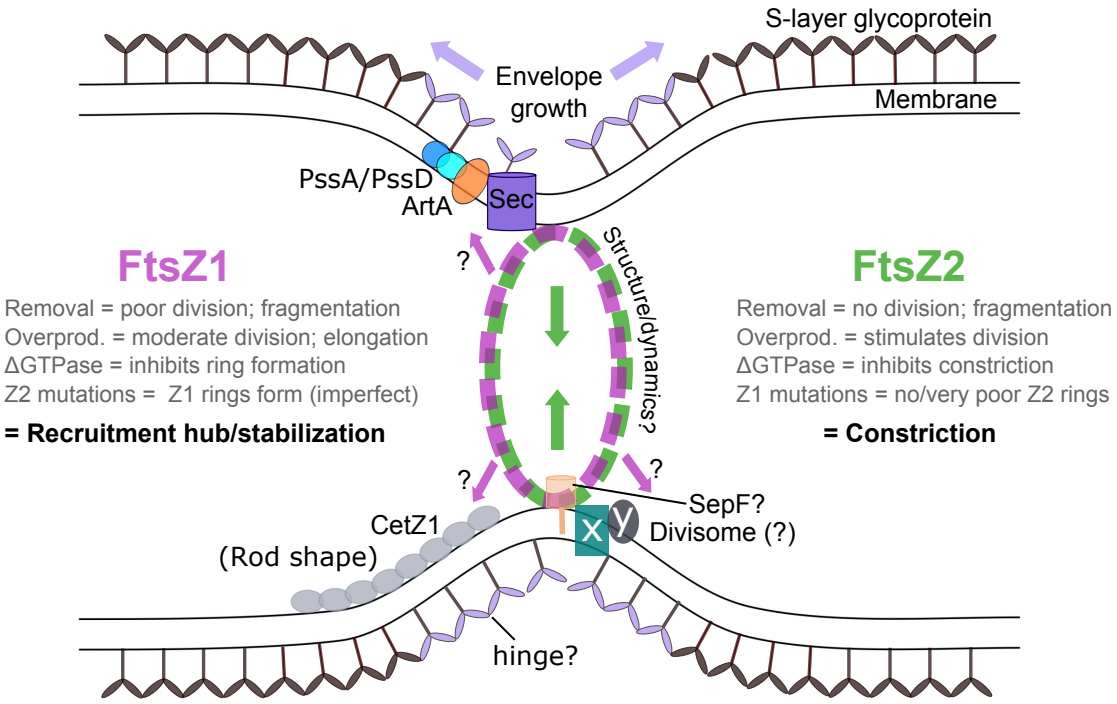

894

895 **Figure 6. Model of FtsZ1 and FtsZ2 function at the archaeal division site**. Schematic
896 models of FtsZ1 (magenta) and FtsZ2 (green) localization and functions (arrows) are based on
897 our results (summarized here). Most archaea, including *H. volcanii*, have an envelope
898 composed of a lipid membrane and an S-layer glycoprotein semi-crystalline array on the
899 surface. Our results raise questions about the ultrastructure and dynamics of the two FtsZ
900 proteins in the division ring, the identity of an unknown number of other putative divisome
901 components (x, y) including a SepF homolog, and how the ring could functionally associate
902 with the envelope growth (Sec/PssA/PssD/ArtA) and cell shape regulation (CetZ1)
903 machineries, which appear to be spatially and functionally linked to midcell[20,41].